HHS Public Access

Author manuscript

*Cell Metab*. Author manuscript; available in PMC 2021 December 01.

Published in final edited form as:

*Cell Metab*. 2020 December 01; 32(6): 967–980.e5. doi:10.1016/j.cmet.2020.10.025.

# Succinyl-CoA Ligase Deficiency in Pro-inflammatory and Tissue-Invasive T Cells

**Bowen Wu**[1], **Jingtao Qiu**[1], **Tuantuan V. Zhao**[1], **Yanan Wang**[1], **Toshihisa Maeda**[1], **Isabel N. Goronzy**[2], **Mitsuhiro Akiyama**[1], **Shozo Ohtsuki**[1], **Ke Jin**[1], **Lu Tian**[3], **Jörg J. Goronzy**[1], **Cornelia M. Weyand**[1,*]

[1]Department of Medicine, Stanford University School of Medicine, Stanford, CA 94305, USA

[2]Stanford University, Stanford, CA 94305, USA

[3]Department of Biomedical Data Science, Stanford University, Stanford, CA 94305, USA

## SUMMARY

Autoimmune T cells in rheumatoid arthritis (RA) have a defect in mitochondrial oxygen consumption and ATP production. Here, we identified suppression of the GDP-forming b subunit of succinate-CoA ligase (SUCLG2) as an underlying abnormality. SUCLG2-deficient T cells reverted the tricarboxylic acid (TCA) cycle from the oxidative to the reductive direction, accumulated α-ketoglutarate, citrate, and acetyl-CoA (AcCoA), and differentiated into pro-inflammatory effector cells. In $AcCoA^{hi}$ RA T cells, tubulin acetylation stabilized the microtubule cytoskeleton and positioned mitochondria in a perinuclear location, resulting in cellular polarization, uropod formation, T cell migration, and tissue invasion. In the tissue, SUCLG2-deficient T cells functioned as cytokine-producing effector cells and were hyperinflammatory, a defect correctable by replenishing the enzyme. Preventing T cell tubulin acetylation by tubulin acetyltransferase knockdown was sufficient to inhibit synovitis. These data link mitochondrial failure and AcCoA oversupply to autoimmune tissue inflammation.

## Graphical Abstract

*Correspondence: cweyand@stanford.edu.

AUTHOR CONTRIBUTIONS

Conceptualization, C.M.W., J.J.G., B.W.; Formal Analysis, B.W., L.T.; Investigation, B.W., J.Q., T.Z., Y.W., T.M., I.N.G., M.A., S.O., K.J.; Writing-original, B.W., C.M.W.; Writing-Review+Editing, C.M.W., J.J.G., B.W.; Supervision, C.M.W., J.J.G.; Funding Acquisition, C.M.W., J.J.G.

SUPPLEMENTAL INFORMATION

Supplemental Information can be found online at https://doi.org/10.1016/j.cmet.2020.10.025.

DECLARATION OF INTERESTS

The authors have declared that no conflict of interest exists.

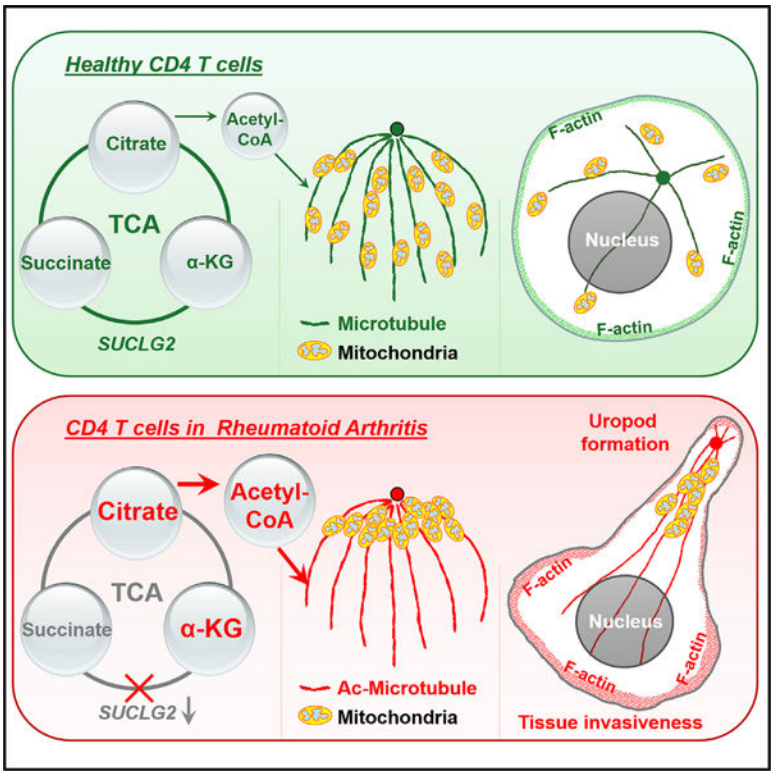



## In Brief

In rheumatoid arthritis, T cells promote chronic-destructive joint inflammation. Wu et al. show that such T cells lack sufficient succinyl-CoA ligase, unbalancing TCA cycle metabolic intermediates. Acetyl-CoA overabundance hyperacetylates tubulin, inducing mitochondrial clustering, cellular polarization, and tissue invasiveness. These data implicate acetyl-CoA in controlling pro-inflammatory T cells in autoimmune disease.


## INTRODUCTION

Rheumatoid arthritis (RA) is a prototypic autoimmune disease with an extended preclinical phase characterized by loss of self-tolerance and autoantibody production (Deane et al., 2010). During clinically apparent RA, innate and adaptive immune cells invade the synovium and together with joint-endogenous cells form tissue-destructive lesions. T cells are key pathogenic drivers required for autoantibody production and sustain synoviocyte proliferation, neoangiogenesis, and cartilage and bone erosions (Slowikowski et al., 2018; Weyand and Goronzy, 2006). Multiple genetic polymorphisms associated with RA risk are implicated in T cell receptor signaling (Fonseka et al., 2017; Terao et al., 2016). Pathogenicity of RA CD4 T cells is linked to tissue invasiveness due to enhanced cell motility combined with invasive membrane ruffles (Shen et al., 2017).

Core abnormalities of RA CD4 T cells relate to reprogramming of the metabolic machinery, already present in naive CD4 T cells (Weyand et al., 2017). Unlike non-lymphoid cells, T cells produce enormous progeny when activated, imposing high demand for biomass

production. Combined triggering of the TCR and costimulatory ligands initiates biosynthesis of precursor molecules and ATP. RA T cells have a defect in mitochondrial function, lowering ATP and ROS generation. Their mitochondrial failure results from insufficient mitochondrial DNA repair, due to loss-of-function of the DNA repair nuclease MRE11A (Li et al., 2019). The $ATP^{low}$ status of RA T cells is aggravated by low glycolytic flux due to suppression of the glycolytic enzyme phosphofructokinase (Yang et al., 2013). Instead, glucose shunts into the pentose phosphate pathway (PPP), driving anabolic metabolism and biomass production (Yang et al., 2016). Excess NADPH and glutathione prevent activation of the redox-sensing kinase ATM, enabling bypassing of cell cycle checkpoints and hyperproliferation (Goronzy and Weyand, 2017). PPP shunting also promotes lipogenesis and the deposition of excessive fatty acids as cytoplasmic lipid droplets (Shen et al., 2017). Favoring a cell building program requires continuous mTORC1 activation and suppression of the energy sensor AMP-activated protein kinase (AMPK). RA T cells achieve this by inhibiting AMPK translocation to the lysosome, promoting unopposed mTORC1 activation. Lysosomal recruitment of AMPK fails due to inefficiency of N-myristoyltransferase 1, the enzyme responsible for adding a lipid tail to AMPK (Wen et al., 2019).

Besides energy production, mitochondria participate in calcium homeostasis, lipid synthesis, apoptosis, and cell cycle progression (Desdín-Micó et al., 2018) and are the major producers of ROS and of metabolic intermediates generated in the TCA cycle. Substrate breakdown in the TCA cycle provides reducing equivalents for oxidative phosphorylation (OXPHOS) but also biosynthetic precursors. Citrate, produced by condensation of acetyl-CoA (AcCoA) and oxaloacetate, is readily exported into the cytoplasm by the citrate transport protein (Gnoni et al., 2009), where it is converted back into oxaloacetate and AcCoA. Cytosolic AcCoA feeds lipid synthesis and serves as a reservoir for posttranslational protein modifications (Choudhary et al., 2014; Icard et al., 2012; Wellen et al., 2009). α-ketoglutarate (α-KG), through which glutamine/glutamate enter the TCA cycle, can undergo reductive carboxylation and leave the mitochondria as citrate (Ward et al., 2010). Two enzymes, oxoglutarate dehydrogenase complex (OGDC) and succinyl coenzyme A synthetase (SCS), consecutively convert α-KG into succinate.

The current study has identified a disruption of the TCA cycle in RA T cells, caused by the loss-of-function of two enzymatic complexes that generate succinate out of α-KG; specifically, OGDC and the GDP-forming β subunit of succinate-CoA ligase (SUCLG2). This TCA cycle roadblock led to reversal of substrate flow, increasing citrate and AcCoA over succinate. Abundance of AcCoA, the sole donor of acetyl groups for protein acetylation, provided sufficient substrate for lysine acetyltransferases to acetylate, and thus stabilize, the microtubule network. In T cells, microtubule stabilization caused cellular polarization, uropod formation, and perinuclear relocation of mitochondria. Through front-rear polarity, the reverse TCA directly regulated T cell motility and tissue invasion. $SCS^{low}$ RA T cells were highly efficient effector cells and drove tissue inflammation. Two interventions restored tissue protection: repair of TCA cycle directionality by SUCLG2 overexpression and prevention of tubulin acetylation by ATAT1 knockdown. Thus, TCA cycle intermediates control T cell migration through microtubule reformatting and uropod formation and link TCA cycle directionality and AcCoA abundance to threshold setting for autoimmune tissue inflammation.

# RESULTS

## Reversal of the TCA Cycle in SUCLG2-Deficient T Cells

CD4 T cells from RA patients are ATP deprived due to three molecular defects: insufficiency of PFK-dependent glycolytic flux, AMPK misplacement, and reduced mitochondrial ATP synthesis. Low ATP concentrations co-exist with elevated NADPH and highly efficient fatty acid synthesis. To understand how RA CD4 T cells diverge energy sources away from ATP production toward biomass production, we quantified metabolic intermediates as well as mitochondrial oxygen consumption. For all experiments, $CD4^+CD45RA^+$ T cells isolated from peripheral blood mononuclear cells (PBMCs) were stimulated for 72 h. Patients with psoriatic arthritis (PsA) served as disease controls. Metabolite concentrations in T cells from PsA patients resembled those from healthy subjects. RA T cells displayed a distinct profile of TCA cycle intermediates (Figures 1A–1D), containing about half the concentration of succinate, and instead accumulating α-KG, citrate, and AcCoA (Figures 1A–1D). The succinate/α-KG ratio was about 10 in healthy T cells and fell to 2 in RA T cells. The shift in the succinate/α-KG ratio was already apparent in resting naive CD4 T cells (Figures S1A and S1B). Overall, the pattern of metabolic intermediates in the patients was suggestive for reductive carboxylation and reverse TCA cycle flux.

Mitochondrial oxygen consumption rates in healthy and patient-derived T cells were compared by Seahorse technology (Figures 1E–1I). Resting RA CD4 T cells consumed 40% less oxygen than healthy T cells (Figure 1F). Maximal respiration and ATP-related oxygen consumption were reduced by 50% in RA T cells (Figures 1G and 1H), with no difference in spare respiratory capacity (Figure 1I). The mitochondrial membrane potential was reduced in RA T cells (Figure 1J). These data suggested mitochondrial malfunction in RA T cells, affecting both oxidative phosphorylation and energy generation from pyruvate oxidation.

We performed transcriptional analysis of the 13 TCA cycle enzymes (Figure 1K). Gene transcripts encoding *DLD* and *SUCLG2* components were significantly repressed in RA T cells (Figure 1L). *DLD* encodes a protein subunit in the oxoglutarate dehydrogenase complex (OGDC) and the *SUCLG2*-encoded protein is part of succinyl-CoA synthetase (SCS). These two enzyme complexes convert α-KG to succinyl-CoA and consecutively to succinate (Johnson et al., 1998). The other SCS beta subunit isoform *SUCLA2* was barely expressed in human T cells (Figure S1C). By immunoblotting, SUCLG2 protein concentrations were markedly reduced in RA T cells (Figure 1M). In RA T cells, catalytic activity of SCS was less than 50% of controls (Figures 1N and 1O).

Lowering of *DLD* and *SUCLG2* transcripts affected both naive and memory CD4 T cells (Figures S1D and S1E). Comparative studies of tissue-residing T cells in rheumatoid synovitis and in giant cell arteritis (GCA) showed strong expression of SUCLG2 protein in GCA T cells and consistently low signals in RA T cells (Figure 1P). In addition to the GCA patients, we enrolled patients with systemic lupus erythematosus (SLE), psoriatic arthritis (PsA), and granulomatosis with polyangiitis (GPA). T cell activation-induced upregulation of *DLD* and *SUCLG2* transcripts in these patients was intact and indistinguishable from age-matched controls (Figures S1F and S1G).

To identify upstream signals regulating *DLD* and *SUCLG2*, healthy naive CD4 T cells were exposed to inflammatory conditions. TNF-α, a key cytokine in RA, and plasma from RA patients failed to lower *DLD/SUCLG2* transcripts (Figures S1H–S1K). Feeding naive CD4 T cells with acetate, a known precursor of cytoplasmic AcCoA (Vysochan et al., 2017), elevated AcCoA concentrations but left *DLD* and *SUCLG2* transcripts unaffected (Figure S1L).

Together, these data identified a mitochondrial defect in RA T cells, leading to a block in oxidative phosphorylation and reductive carboxylation, reversing TCA cycle progression. Transcriptional repression of two successive enzymes needed for the α-KG to succinate conversion produced a distinguishing metabolic signature of $AcCoA^{high}$/ $citrate^{high}$/ $succinate^{low}$ in RA T cells.

## *SUCLG2* Loss-of-Function Is Sufficient to Produce the Metabolic Phenotype of RA T Cells

*SUCLG2* encodes for the GTP-specific b subunit of succinyl-CoA synthetase (SCS), a mitochondrial matrix enzyme with three substrates: GTP, CoA, and succinate (Johnson et al., 1998). No humans with *SUCLG2* mutations have been reported, suggesting lethality associated with SUCLG2 deficiency. Mutations in other SCS components lead to mitochondrial DNA depletion syndrome and mitochondrial failure.

To investigate whether impaired respiration and shifted metabolite generation in RA T cells were caused by SUCLG2 deficiency, we applied a gain-of-function and loss-of-function approach. Partial *SUCLG2* silencing in healthy T cells (Figure S2A) reproduced the RA T cell phenotype (Figures 2A–2E). Vice versa, SUCLG2 was reconstituted in RA T cells by transfection of a *SUCLG2* overexpression construct (Figure S2B). Manipulation of SUCLG2 expression did not significantly affect cell viability (Figures S2C and S2D). Oxygen consumption in healthy T cells was highly sensitive to *SUCLG2* knockdown (Figures 2A–2C), which reduced basal oxygen consumption by >50% and maximal respiration by 70%. Targeting *SUCLG2* with a second siRNA oligo yielded similar results (Figures S2E–S2G). *SUCLG2* loss-of-function decreased intracellular succinate levels (Figure 2D), prompted AcCoA accumulation (Figure 2E), and suppressed the mitochondrial membrane potential (Figure S2H). Conversely, repair of SUCLG2 expression in RA T cells markedly enhanced mitochondrial respiration (Figures 2F–2H); basal OCR and maximal respiration doubled, and the mitochondrial membrane potential improved (Figure S2I). Also, enforced *SUCLG2* expression in RA T cells elevated intracellular succinate (Figure 2I) and lowered AcCoA concentrations (Figure 2J).

In summary, SUCLG2 loss-of-function in RA T cells leads to a severe metabolic phenotype due to the key role of SCS in generating succinate, supplying the electron transport chain, and regulating the intracellular AcCoA pool.

## SUCLG2-Deficient T Cells Are Inflammatory

CD4 T cells are key drivers of rheumatoid tissue inflammation (Rao et al., 2017; Weyand and Goronzy, 2006). To mechanistically link SUCLG2 expression and functional behavior of synovial T cells, we exploited a human synovium-NSG mouse chimera model. Adoptive transfer of RA PBMCs into NSG mice engrafted with human synovium predictably leads to

synovitis (Li et al., 2016; Shen et al., 2017). We transfected isolated CD4 T cells from RA PBMCs with a *control* or *SUCLG2* expression plasmid (Figure 3A). Control mice were engrafted with synovial tissue but did not receive PBMCs. Eight synovial explants in each group were analyzed by H&E and dual-color immunofluorescence staining. The tissue transcriptome was examined by RT-PCR. Restoring *SUCLG2* expression in RA CD4 T cells profoundly affected tissue inflammation. Adoptively transferred RA PBMCs induced robust synovitis (Figure 3B). Normalizing SUCLG2 expression selectively in CD4 T cells mitigated the pro-inflammatory potential, markedly lowering the density of the tissue infiltrates (Figure 3B). Since the intensity of synovitis is closely correlated to the presence of IFN-γ-producing T cells, we quantified IFN-$\gamma^+$ T cells in the tissue sections by CD3/IFN-γ dual color immunofluorescence. Adoptive transfer-induced synovitis was associated with the recruitment/retention of IFN-$\gamma^+$ T cells (Figures 3C and 3D). SUCLG2 reconstitution selectively in transferred CD4 T cells markedly reduced the abundance of tissue-residing IFN-$\gamma^+$ T cells (Figures 3C and 3D). Tissue transcriptome analysis confirmed the functional relevance of *SUCLG2* expression in CD4 T cells. Infusion of RA PBMCs resulted in high expression of *TCR*, *TBET*, and *RORG* transcripts, indicative of T cells committed to the Th1 or Th17 lineage (Figure 3E). Concomitantly, synovial tissues from chimeras that had received RA PBMCs transfected with the control plasmid contained high amounts of effector cytokine transcripts, including *IFNG, IL17*, and *IL21* (Figure 3F). Restoring SUCLG2 expression in RA CD4 T cells prior to adoptive transfer significantly lowered *TCR, TBET*, and *RORG* expression and transcripts for all inflammatory cytokines declined significantly (Figure 3F). The anti-inflammatory cytokines IL-10 and TGF-β were unaffected by any of the interventions.

Taken together, SUCLG2-deficient T cells induce tissue inflammation, and correction of this metabolic defect is sufficient to reestablish tissue protection.

## Excess AcCoA Leads to Tubulin Hyperacetylation

The major metabolic consequences of *DLD* and *SUCLG2* deficiency and TCA cycle reversal are the accumulation of citrate and AcCoA. AcCoA promotes IFN-γ production via epigenetic regulation of the *IFNG* locus (Peng et al., 2016), and AcCoA accumulation during viral infection enhances rapid memory CD8 T cell responses (Balmer et al., 2016). To examine whether surplus AcCoA in RA T cells interferes with T cell differentiation, we increased cellular AcCoA concentrations by culturing T cells in the AcCoA donor acetate. Only high acetate concentrations shifted CD4 T cells to IFN-γ production (Figure S3A). Similarly, manipulating SUCLG2 expression, by siRNA-mediated knockdown or plasmid-induced overexpression, increased and decreased the frequency of IFNG-$\gamma^+$ T cells, respectively, compatible with AcCoA-dependent shifts in T cell differentiation (Figures S3B and S3C).

In search of additional functional consequences of AcCoA pool expansion, we considered that AcCoA donates acetyl groups for post-translational modification of proteins. A possible target protein is the cytoskeletal protein tubulin in which acetylation leads to microtubule stabilization (Matsuyama et al., 2002). We quantified acetylated tubulin (Ac-tubulin) in CD4 T cells by cytofluorometry, immunoblotting, and single-cell imaging (Figures 4A–4F). Ac-

tubulin was easily detectable in stimulated CD4 T cells and was consistently at higher abundance in RA T cells. Flow cytometry for α-tubulin K40 acetylation demonstrated significantly higher concentrations in RA T cells (Figure 4B). By western blotting, acetylated tubulin was more than twice as high in RA compared to control cells (Figure 4D). Single-cell immunofluorescence demonstrated high Ac-tubulin expression in almost 50% of the RA T cells (Figure 4F), while cellular tubulin concentrations were unchanged (Figure S4A). The major acetyltransferase for tubulin is α-tubulin acetyltransferase-1 (ATAT1), and HDAC6 is the corresponding deacetylase (Sadoul and Khochbin, 2016). Based on gene expression studies, control and RA T cells expressed similar transcript levels (Figure 4G), excluding enzyme abundance as the key contributor to tubulin hyperacetylation.

We tested whether SUCLG2 expression can alter the microtubular cytoskeleton. *SUCLG2* knockdown in healthy T cells significantly increased tubulin acetylation (Figures 4H–4I). Restoration of SUCLG2 in $AcCoA^{high}$ RA T cells prevented tubulin hyperacetylation (Figures 4J and 4K). Mitochondrial inhibition with antimycin A/rotenone promptly increased ac-tubulin (Figures 4L–4N). Lipoic acid is a co-factor of the pyruvate dehydrogenase complex and enhances mitochondrial AcCoA production (Hassan and Cronan, 2011). Culture of healthy T cells in lipoic acid-rich medium enhanced ac-tubulin (Figures 4O–4Q). Mitochondrial citrate export requires the citrate transport protein (CTP) (Gnoni et al., 2009). Treatment of RA T cells with the CTP inhibitor CNASB promptly reduced tubulin acetylation (Figures 4R–4T). Citrate oversupply results in accelerated lipid synthesis (Figure S4B) and formation of cytoplasmic lipid droplets (Shen et al., 2017). We visualized lipid droplets and tubulin acetylation by Bodipy/Ac-tubulin co-staining. RA T cells accumulated lipid droplets and the amount correlated with the intensity of tubulin acetylation (Figures S4C and S4D).

Thus, AcCoA overabundance in SUCLG2-deficient T cells was dependent on citrate transport and resulted in hyperacetylation of the microtubule system.

## Tubulin Hyperacetylation Enhances T Cell Motility and Tissue Invasiveness

In RA, T cells mediate their pathogenic function by infiltrating into synovial tissue. To mechanistically connect AcCoA-induced hyperacetylation with migratory behavior, we compared the invasive ability of healthy and RA T cells in 3D collagen gels and in transwell migration assays. RA T cells were more efficient than controls to enter the collagen matrixes and penetrate into deeper layers (Figures 5A–5C). In transwell chambers, twice as many RA T cells migrated compared to controls (Figure 5D). We inhibited microtubule organization with nocodazole (Figures S5A–S5C), which disrupted the invasive behavior of RA T cells in 3D collagen gel and in the transwell migration system. We compared Ac-tubulin concentrations in migrating (lower chamber) and non-migrating (upper chamber) T cells (Figures 5E–5G). Migrated T cell populations consistently had higher Ac-tubulin levels by flow cytometry (Figure 5F) and by confocal microscopy (Figure 5G). The invasive ability was dependent on tubulin acetylation, as demonstrated in *ATAT1* knockdown experiments (Figures 5H–5J). To examine whether tubulin hyperacetylation also affects T cell differentiation and effector function, we enforced tubulin hyperacetylation in healthy CD4 T cells by ATAT1 overexpression (Figures S6A and S6B). Lineage-determining transcription

factors (Figure S6C) and frequencies of IFN-γ and IL-17-producing T cells (Figure S6D) remained unchanged.

To investigate tissue invasion *in vivo*, we exploited the humanized mouse model presented in Figure 3. PBMCs were transfected with *ATAT1* or control siRNA prior to the transfer into the human synovium-NSG chimeras. Synovial grafts were explanted, and tissue expression of inflammatory genes was profiled by RT-PCR (Figure 5K). All tissue explants in the control group had high expression of *IFNG*, *IL17*, *IL1B*, *IL6*, and *TNFA* transcripts. The lineage-determining transcription factors *TBX21* and *RORC* were strongly upregulated. Loss of the acetylating enzyme profoundly affected the tissue lesions. Tissue transcriptome analysis in mice reconstituted with *ATAT1* siRNA transfected PBMCs showed low abundance of essentially all inflammatory gene transcripts (Figure 5K). Also, the density of tissue-infiltrating T cells was markedly reduced (Figure 5L). Immunohistochemical staining of tissue sections confirmed the anti-inflammatory effect of *ATAT1* silencing. Control grafts contained dense T cell infiltrates, while T cell density was significantly reduced after *ATAT1* knockdown (Figures 5M and 5N). Tissue-invasive T cells often were arranged in clusters, mimicking rheumatoid synovitis. T cell clustering was typical in the control grafts and much less frequent after *ATAT1* loss-of-function (Figure 5O).

These experiments implicated stabilized tubulin in T cell behavior, specifically in tissue invasiveness and mechanistically coupled mitochondrial intactness to cytoskeletal function and T cell fitness.

## SUCLG2 Deficiency Controls Cellular Shape and Uropod Formation

T cells are highly mobile cells that move through amoeboid migration (Lämmermann and Sixt, 2009). Cellular motion requires polarization of cell contents into segregated front and rear environments and positioning of energy production close to rear-positioned actomyosin. We tested whether RA T cells form separated subcellular compartments (Figures 6A and 6B) by measuring the Golgi apparatus-nucleus distance. On collagen-coated surfaces, Ac-tubulin$^{high}$ RA T cells spontaneously elongated, yielding an average Golgi-nucleus distance of 5 μm (control; 2 μm) (Figure 6B). To delineate the dependence of T cell polarization on Ac-tubulin, we knocked down *ATAT1*. In ATAT1$^{lo}$ T cells, the Golgi was placed less than 1 μm away from the nucleus, connecting Golgi movement to Ac-tubulin (Figures 6C and 6D).

Morphologic changes leading to uropod formation can be captured by cell circularity. To optimize conditions for cell motion, we placed healthy and RA T cells onto an endothelial monolayer (Figures 6E and 6F). Most healthy T cells appeared round, with an average circularity index of 0.85 (1.0 identifying ideal circles). Conversely, RA T cells spontaneously adopted to an elongated phenotype with an average circularity index of 0.65. Cell shape was dependent on Ac-tubulin, as revealed by *ATAT1* knockdown (Figures 6G and 6H). Most RA T cells rounded up after *ATAT1* knockdown, shifting average cell circularity from 0.7 to 0.82 (Figures 6G and 6H).

To characterize the uropods of RA T cells, we stained for the centrosome marker pericentrin, F-actin, and lipid droplets (Figures S7A–S7C). As the microtubule organizing center (MTOC), centrosome location determines the direction of the tubulin microtubule system. In

the spontaneously polarized RA T cells, centrosomes detached from the nucleus and located near the tip of the uropod, indicating significant reorientation of microtubules. Lipid droplets accumulated in the uropod, while F-actin was redistributed close to the cytoplasmic membrane.

Taken together, these data revealed that TCA cycle activity regulates front and rear cytoskeletal elements via AcCoA production, determining cell shape, uropod formation, and organelle placement.

### SUCLG2 Deficiency and Tubulin Hyperacetylation Facilitate Perinuclear Mitochondrial Clustering

The subcellular distribution of mitochondria determines local concentrations of metabolites, ATP, ROS, and calcium, linking mitochondrial positioning with signaling function (Desdín-Micó et al., 2018; Eisner et al., 2018; Schwindling et al., 2010). We tested whether microtubular acetylation affects mitochondrial placement. The distribution of $HSP60^{+}$ mitochondria was fundamentally different in control and RA T cells (Figure 7A). In RA T cells, mitochondria polarized to one cellular pole, co-localizing with acetylated tubulin. In healthy T cells, mitochondria diffusely distributed throughout the cytoplasm. We developed a mitochondrial polarization index (MPI) by subdividing the cell into eight sections and comparing signal intensities. Single-cell analysis of the MPI demonstrated the propensity of RA T cells to place mitochondria in perinuclear clusters (Figures 7B and 7C). Treatment of T cells with the mitochondrial inhibitor antimycin/ rotenone redistributed mitochondria to the perinuclear rim (Figures 7D and 7E). To implicate microtubules in mitochondrial positioning, we knocked down *ATAT1* in RA T cells. Decreased tubulin acetylation dispersed mitochondria across the cytoplasm (Figures 7F and 7G). Promoting tubulin hyperacetylation in healthy T cells via *ATAT1* overexpression or lipoic acid treatment mimicked the mitochondria distribution pattern in RA T cells (Figures 7H–7K).

Collectively, these data implicated TCA directionality, AcCoA production, and posttranslational modification of the cytoskeleton in controlling the placement of mitochondria in a nucleus-proximal position.

## DISCUSSION

IFN-γ-producing CD4 T cells are characteristic effector cells in the synovium and blood of RA patients (Fonseka et al., 2018). Supporting autoantibody-producing B cells, tissue-residing CD4 T cells display features of follicular helper T cells (Zhang et al., 2019). How they acquire their pathogenic state is not understood, but recent data have revealed a fundamental metabolic reprogramming of CD4 RA T cells (Weyand et al., 2017) relevant for lymph node-residing and synovia-infiltrating T cells (Weyand and Goronzy, 2020;). Current data explored underlying molecular defects in such T cells and identified the mitochondrial matrix enzyme succinate-CoA ligase as a key regulator of T cell behavior. Specifically, in RA CD4 T cells, SUCLG2 transcription was repressed, interrupting the formation of succinate from succinyl-CoA. Metabolic consequences included TCA cycle reversal and accumulation of α-KG, citrate, and AcCoA. AcCoA overabundance had profound implications for T cell functions, all of which are critically involved in rendering T cell pro-

inflammatory and arthritogenic. Loss-of-function and gain-of-function experiments confirmed SUCLG2's key role in the inflammatory potential of CD4 T cells. SUCLG2 overexpression in RA T cells was sufficient to suppress synovial inflammation *in vivo*, placing the TCA cycle enzyme into a key position in regulating tissue inflammation.

Impaired α-KG to succinate conversion and reversal of TCA directionality was typical for tissue-residing T cells, but more importantly, was already present in naive CD4 T cells, where it resulted in a differentiation defect that directed T cells to differentiate into short-lived effector T cells (SLECs) instead of memory precursor cells (MPECs). *In vivo*, such SLECs rapidly entered synovial tissue and induced aggressive synovitis. SLECs live in a relatively energy-deprived state, as they redirect energy carriers away from ATP generation toward biomass generation. SLECs are hyperproliferative and hypermobile, as opposed to more stationary MPECs that secure immunologic memory by restraining clonal expansion. In essence, we have identified the metabolic origins of a deviation in T cell differentiation that translates into the breakdown of tissue tolerance.

Experiments presented here identified SUCLG2 as an upstream defect in the mitochondrial dysfunction of RA T cells resulting in mitochondrial and cytoplasmic AcCoA accumulation. AcCoA is critical to multiple cellular processes, including the donation of the acetyl moiety for posttranslational protein modifications. Current data linked the metabolic status of T cells to the functionality of their microtubules, hollow and polarized tubes assembled from α and β-tubulin heterodimers. α-tubulin K40 acetylation, rapidly achieved in $AcCoA^{hi}$ T cells, is restricted to tubulin subunits incorporated into the microtubule lattice (Janke and Montagnac, 2017) and requires the tubulin acetyltransferase ATAT1. α-tubulin acetylation enhances microtubule flexibility and mechanical stress resistance (Portran et al., 2017; Xu et al., 2017). We predicted that T cell functions dependent on cellular reshaping would be most sensitive to AcCoA surplus and confirmed that $AcCoA^{hi}$ RA T cells spontaneously formed a uropod, preparing them for highly efficient tissue invasion.

Like neutrophils, but distinct from fibroblasts and other mesenchymal cells, T cells use amoeboid movements to migrate out of blood vessels and into the tissue extracellular space. Amoeboid migration is rapid and independent from proteolytic matrix degradation but requires a highly contractile rear uropod. RA T cells spontaneously formed a uropod and leading edge podosome-like structures rendering them invasive (Shen et al., 2017). Current data link metabolic programming to rear end formation and cell polarity. Rho GTPase signaling defines structural arrangements at the leading edge and the uropod (Hind et al., 2016), but polarized morphology and rear end contractility appear to depend on microtubular acetylation. Reduced ATP production should signal energy deprivation and force the T cell to pause. However, due to TCA cycle redirection, RA T cells generate excess citrate and AcCoA, compatible with a state of pseudoenergy supply, that translates into excessive migratory activity.

Post-translational modifications function as guides for molecular motors, targeting cargo to defined subcellular regions (Konishi and Setou, 2009). Mitochondrial distribution patterns include subplasmalemmal, pan-cytoplasmic, or perinuclear positioning (Bavister, 2006; Katayama et al., 2006), with subplasmalemmal mitochondria in the immunologic synapse

functioning as a local calcium sink (Quintana et al., 2006). Microtubule-dependent mitochondrial placement determines local concentrations of metabolites and reactive oxygen species. Perinuclear mitochondrial clustering creates an oxidant-rich nuclear domain (Al-Mehdi et al., 2012). RA T cells pulled mitochondria to the perinuclear region and mitochondria in healthy T cells rapidly moved to this location with AcCoA excess. In RA T cells, reductive elements are abundant (Yang et al., 2016) but dysfunctional perinuclear mitochondria may nevertheless create local oxidative stress affecting nuclear regulation.

If T cell mobility, tissue invasiveness, and pro-inflammatory propensity are ultimately determined by TCA cycle progression and metabolic intermediates, metabolic interference could potentially restore tolerance. The RA disease process begins decades prior to joint inflammation (Demoruelle et al., 2014). Notably, mitochondrial abnormalities affect lymph node CD4 T cells of RA patients, similar to HIV infection (Li et al., 2019). Mitochondrial failure, induced by the loss of the DNA repair nuclease MRE11A, triggers cytoplasmic leakage of mtDNA, inflammasome activation, and ultimately, pyroptotic T cell death. T cells dying a lytic death may provide the strongest inflammatory stimulus, identifying their tissue invasiveness as a key checkpoint in tissue deprotection. T cell migratory behavior relied on the state of the microtubular system and was therefore targetable by blocking ATAT1. Similarly, inhibiting citrate export out of the mitochondria, critical in AcCoA transport to the cytoplasm, where it gains access to α-tubulin, reduced the acetylation of the microtubular lattice. *In vivo*, ATAT1 loss-of-function was sufficient to inhibit tissue inflammation. These data raise the possibility that metabolic interference can target key abnormalities in T cells and represents a potentially novel strategy for immunomodulatory therapy.

### Limitations of Study

The study implicates TCA cycle intermediates in T cell fate regulation and in tissue inflammation. Mechanisms leading to SUCLG2 suppression as the underlying cause of TCA reversal remain undefined. Also, we have linked AcCoA overabundance to tubulin hyperacetylation, but it is likely that other cytoplasmic and nuclear proteins are similarly modified, affecting other functional domains of T cells. Finally, functional implications of perinuclear mitochondrial clustering and how this translates into T cell misbehavior should be explored. Further studies need to examine whether dysregulated protein acetylation is a disease mechanism relevant in other chronic inflammatory conditions.

## STAR*METHODS

### RESOURCE AVAILABILITY

**Lead Contact—**Further information and requests for resources and reagents should be directed to and will be fulfilled by the Lead Contact, Cornelia M. Weyand (cweyand@stanford.edu).

**Materials Availability—**This study did not generate new unique reagents.

**Data and Code Availability—**There are neither new datasets/code generated nor restrictions for use of the materials in the paper.

## EXPERIMENTAL MODEL AND SUBJECT DETAILS

**Patients and Tissues—**Patients with a diagnosis of RA (n = 162; age: 50.0 ± 15.7 years; 76% females) were recruited into the study and donated a peripheral blood sample. All RA subjects fulfilled the diagnostic criteria for RA and were positive for rheumatoid factor and/or anti-CCP. In addition, synovial tissue samples were collected from 14 patients (age: 58.6 ± 13.0 years; 50% females). Patients with a diagnosis of PsA (n = 17; age: 59.0 ± 9.2 years; 41.2% females) served as disease controls. Clinical characteristics of RA and PsA patients are given in Table S1. In a study comparing the gene expression of *SUCLG2* in activated $CD4^+$ T cells, male and female patients were not different. Age-matched healthy donors without a personal history of cancer or autoimmune disease were enrolled as healthy controls. Individuals with cancer, uncontrolled medical disease or any other inflammatory syndrome were excluded. Appropriate informed consent was obtained, and all protocols were approved by the Stanford Institutional Review Board.

**Cell Preparation and Culture—**Peripheral blood mononuclear cells (PBMCs) were isolated by gradient centrifugation with Lymphocyte Separation Medium (Lonza). $CD4^+CD45RA^+$ naive T cells were purified by negative selection with the EasySep Human Naive CD4 T Cell Enrichment Kit (STEMCELL Technologies). Purity of cell populations was consistently > 95%. To activate naive CD4 T cells, anti-CD3/anti-CD28-coated beads (Life Technologies AS) were used at a ratio of 2 cells: 1 bead for 72 h.

**Human Synovial Tissue–NSG Mouse Chimeras—**NOD.Cg-PrkdcscidIl2rgtm1Wjl/SzJ (NSG) mice (Jackson Laboratory) were maintained and bred under specific pathogen-free conditions on a 12/12 h light/dark cycle at 20–22°C with free access to water and food (Teklad Global Rodent Diet (Envigo 2018S)). Animal housing facilities were monitored for infection with specific pathogens every 6 weeks and the health status of all animals was checked on a daily basis. As previously described, (Li et al., 2016; Shen et al., 2017; Yang et al., 2016), pieces of human synovial tissue were subcutaneously implanted in 8–12-week old mice. Synovial tissues were collected from synovectomies or arthroplasties and margins without visible inflammation were deemed appropriate for engraftment. After 7 days, the mice were reconstituted with 10 million RA PBMC. Littermates (both males and females) were used for each independent experiment and randomly assigned to the different experimental groups. In a series of experiments, CD4 T cells were isolated by FACS sorting, transfected with *SUCLG2* overexpression plasmids or control vectors, remixed with the CD4 T cell-depleted PBMC and adoptively transferred into the mice. To inhibit tubulin hyperacetylation, PBMCs were transfected with siRNA targeting ATAT1 or control siRNA. On day 14, synovial tissues were explanted, OCT-embedded (4583; Sakura Finetek USA) or shock-frozen for further experiments (tissue staining and RNA extraction). To reduce variability introduced by the tissue source and the adoptively transferred immune cells, all mice within one experimental series carried tissue from the same donor patient. All animal studies were approved by the Stanford APLAC Committee and carried out in accordance with the guidelines of the Institutional Animal Care and Use Committee at Stanford University.

## METHOD DETAILS

**T Cell Transfections—**The Human T Cell NucleofectorTM Kit (Lonza, Catalog #: VPA-1002) was used to overexpress or knockdown specific genes in T cells. Prior to transfection, $CD4^+CD45RA^+$ T cells were stimulated with anti-CD3/anti-CD28-coated beads and cultured for 2 days to ensure appropriate activation. On day 2, the T cells were transfected and rested for 24 h to recover from the electroporation. On day 4, cells were used for molecular and functional analyses.

**Metabolic Intermediates Quantification—**$CD4^+CD45RA^+$ naive T cells were stimulated with anti-CD3/anti-CD28-coated beads and cultured for 72 h. α-Ketoglutarate Color-imetric/Fluorometric Assay Kit (BioVision), Succinate Assay Kit (BioAssay Systems), Citrate Assay Kit (Sigma-Aldrich), Acetyl-CoA Assay Kit (Sigma-Aldrich), Free Fatty Acid Quantification Assay Kit (Abcam) were used to measure intracellular α-ketoglutarate, succinate, citrate, acetyl-CoA and free fatty acids.

**Seahorse Assay—**The Seahorse XF Cell Mito Stress Test Kit (Seahorse Biotech cat#: 103015-100) was used to measure mitochondrial oxygen consumption rates, following the manufacturer's instructions. T cells were plated in a 96-well Seahorse assay plate at a confluency of 0.2 million cells per well. The cells were attached to the plate using Cell-Tak (Corning cat#: 354240) and incubated in 37°C for 30 min in a $CO_2$-free incubator in unbuffered RPMI 1640 medium. The cells were treated with oligomycin (1.5 mM), FCCP (1.5 mM), and Rotenone/Antimycin A (0.5 mM), respectively at time-points indicated.

**Mitochondria Membrane Potential Assay—**$CD4^+CD45RA^+$ naive T cells were stimulated with anti-CD3/anti-CD28-coated beads and cultured for 72 h, then stained with MitoTracker Red (Thermo Fisher Scientific) and analyzed with an LSR II flow cytometer (BD Biosciences). Data were analyzed with FlowJo software (Tree Star Inc).

**Real Time PCR—**Total RNA was extracted with Trizol (Thermo Fisher Scientific) and Direct-zol RNA MiniPrep Kit (ZYMO Research). cDNA was synthesized using Maxima First Strand cDNA Synthesis Kits for qPCR with reverse transcription (RT-qPCR) (Thermo Fisher Scientific). Quantitative PCR analyses were performed using SYBR Green qPCR Master Mix (Bimake) and gene expression was normalized to β-actin. Primers are listed in Table S2.

**Immunoblotting—**Cellular proteins were extracted with RIPA buffer (Sigma-Aldrich). Protein expression levels were examined by western blotting as previously described (Yang et al., 2016). Briefly, cells were lysed in lysis buffer and proteins were resolved by 4%–15% SDS-PAGE (Bio-Rad, 4561083). Proteins were then transferred to PVDF membranes (Bio-Rad, 1620177) followed by incubation with 5% milk in TBST blocking buffer for 1 h and incubation with antibody overnight. HRP-conjugated secondary antibody and SuperSignal West Femto Maximum Sensitivity Substrate (Thermo Fisher Scientific 34094) were used to detect protein. SUCLG2 monoclonal antibody was purchased from Santa Cruz Biotechnology, Acetyl-α-tubulin (Lys40) monoclonal antibody was from Thermo Fisher Scientific, α-tubulin monoclonal antibody was from Cell signaling technology. β-Actin

expression detected with anti-β-actin (Cell Signaling Technology, 8H10D10) served as the internal control.

**Succinyl-CoA Synthetase (SCS) Activity Assay—**$CD4^+CD45RA^+$ naive T cells were stimulated for 72 h. Succinyl-CoA Synthetase (SCS) Activity Assay Kit (Abcam) was used to measure SCS activity.

**Immunohistochemistry—**Frozen sections of synovial tissues were stained with mouse anti-human CD3 (1:50; DAKO, Clone F7.2.38) and rabbit anti-human IFN-γ (1:100, Abcam, ab25101). Alexa Fluor 594 anti-mouse IgG (1:200, Thermo Fisher Scientific, A-11032) and Alexa Fluor 488 anti-rabbit IgG (1:200, Thermo Fisher Scientific, A-11034) were used as secondary antibodies. Images of CD3/IFN-γ staining was obtained using a LSM710 confocal microscope (Carl Zeiss) with a Plan-Neofluar × 40/1.3-NA oil objective lens.

**Immunofluorescence—**To visualize intracellular proteins, immunofluorescence staining was applied using primary antibodies and appropriate fluorescent secondary antibodies. The following primary antibodies were used: Acetyl-alpha Tubulin (Lys40) mouse mAb (1:100, Thermo Fisher Scientific), α-tubulin rabbit mAb (1:100, Cell signaling technology), GM-130 rabbit mAb (1:100, Cell signaling technology), Pericentrin rabbit pAb (1:100, Abcam), Hsp60 rabbit mAb (1:100, Cell signaling technology). The following secondary antibodies were used: Alexa Fluor 594 goat anti-mouse IgG (1:200, Thermo Fisher Scientific, A-11032), Alexa Fluor 488 goat anti-rabbit IgG (1:200, Thermo Fisher Scientific, A-11008). Nuclei were stained with DAPI. The LSM710 system (Carl Zeiss) with a Plan Apochromat 63 × /1.40-NA oil DICIII objective lens (Carl Zeiss) was used to acquire images.

**Flow Cytometry—**To measure tubulin acetylation using flow cytometry, $CD4^+CD45RA^+$ naive T cells were stimulated for 72 h. 4% PFA was used for fixation and 0.1% saponin was used to permeabilize the cells. Cells were stained with primary anti-acetyl-alpha tubulin (Lys40) mouse mAb (1:100, Thermo Fisher Scientific) and secondary Alexa Fluor 594 goat anti-mouse IgG (1:200, Thermo Fisher Scientific, A-11032). Flow cytometry was performed on an LSR II flow cytometer (BD Biosciences). Data were analyzed with FlowJo software (Tree Star Inc).

**3D-collagen Invasion Assay—**$CD4^+CD45RA^+$ naive T cells were stimulated for 72 h. $5 \times 10^4$ T cells were seeded on top of a 3D collagen matrix (1.5 mg/mL, bovine collagen type I, Advanced Biomatrix; approximately 5 mm in thickness). After 48 h, collagen matrix was fixed with 4% PFA and stained with DAPI for 1 h. Collagen matrix were imaged with an LSM710 microscope with an EC Plan-Neofluar 10 × /0.3-NA (numerical aperture) DICI objective lens (Carl Zeiss). Z stacks were set to capture images from the surface to the bottom of the 3D collagen matrix.

**Transwell Migration Assay—**$CD4^+CD45RA^+$ naive T cells were stimulated for 72 h. $1 \times 10^5$ cells were cultured in cell culture inserts (PITP01250, Millipore Sigma) with 400 μl of RPMI 1640 medium placed in 12-well plates that contained 600 ml of RPMI 1640 medium.

After 24 h, cells in and out of the inserts were collected and counted, and migration rates were calculated.

**Mitochondria Clustering Quantification—**$CD4^+CD45RA^+$ naive T cells were stimulated for 72 h. Mitochondria marker protein HSP60 was visualized by immunofluorescence staining. Confocal microscopy images for individual cells were divided into 8 parts, and fluorescence intensity of each part was recorded as $I_i$ ($1 \le i \le 8$), total fluorescence intensity of each cell was normalized as 100, $\sum li = 100$, and mitochondria clustering index was defined as $[\sum_{j<i}(li - lj)^2]/28$.

**Cellular Circularity Measurement—**$CD4^+CD45RA^+$ naive cells were stimulated for 72 h. $1 \times 10^4$ T cells were seeded onto HUVECs in 24 well plates for 15 min and then fixed with 4% PFA for 15 min. Bright field images were taken and analyzed using ImageJ software. Cellular outlines were traced using Freehand Selection mode, and cellular circularity was calculated.

### QUANTIFICATION AND STATISTICAL ANALYSIS

Statistical Analysis were done using GraphPad Prism software (GraphPad Software). To compare data within two groups, the paired Wilcoxon test or the Mann-Whitney test were used when the sample size per group was > 5. Parametric t test was used if the sample size per group was ≤ 5, the data values followed a normal distribution and met the assumptions of the test. To adjust for multiple testing, in addition to individual p values, we used Hochberg's step-down method to control for a family-wise-error rate at the 0.05 levels. One-way ANOVA was used and pairwise comparison using Tukey's method was applied for comparisons between 3 or more groups. All data points were included in the analysis and no outliers were detected using Grubbs' test. All data are presented as mean ± SEM. *p < 0.05, **p < 0.01, ***p < 0.001 and statistical parameters can be found in the figure legends.

## Supplementary Material

Refer to Web version on PubMed Central for supplementary material.

## ACKNOWLEDGMENTS

This work was supported by the National Institutes of Health (R01AR042527, R01AI108906, R01HL142068, and P01HL129941 to C.M.W. and I01BX001669, R01AI108891, R01AG045779, U19AI057266, and R01AI129191 to J.J.G.) and by the Encrantz Family Discovery Fund.

## REFERENCES

Al-Mehdi AB, Pastukh VM, Swiger BM, Reed DJ, Patel MR, Bardwell GC, Pastukh VV, Alexeyev MF, and Gillespie MN (2012). Perinuclear mitochondrial clustering creates an oxidant-rich nuclear domain required for hypoxia-induced transcription. Sci. Signal 5, ra47. [PubMed: 22763339]

Balmer ML, Ma EH, Bantug GR, Grählert J, Pfister S, Glatter T, Jauch A, Dimeloe S, Slack E, Dehio P, et al. (2016). Memory CD8(+) T Cells Require Increased Concentrations of Acetate Induced by Stress for Optimal Function. Immunity 44, 1312–1324. [PubMed: 27212436]

Bavister BD (2006). The mitochondrial contribution to stem cell biology. Reprod. Fertil. Dev 18, 829–838. [PubMed: 17147931]

Choudhary C, Weinert BT, Nishida Y, Verdin E, and Mann M (2014). The growing landscape of lysine acetylation links metabolism and cell signalling. Nat. Rev. Mol. Cell Biol 15, 536–550. [PubMed: 25053359]

Deane KD, Norris JM, and Holers VM (2010). Preclinical rheumatoid arthritis: identification, evaluation, and future directions for investigation. Rheum. Dis. Clin. North Am 36, 213–241. [PubMed: 20510231]

Demoruelle MK, Deane KD, and Holers VM (2014). When and where does inflammation begin in rheumatoid arthritis? Curr. Opin. Rheumatol 26, 64–71. [PubMed: 24247116]

Desdín-Micó G, Soto-Heredero G, and Mittelbrunn M (2018). Mitochondrial activity in T cells. Mitochondrion 41, 51–57. [PubMed: 29032101]

Eisner V, Picard M, and Hajnóczky G (2018). Mitochondrial dynamics in adaptive and maladaptive cellular stress responses. Nat. Cell Biol 20, 755–765. [PubMed: 29950571]

Fonseka CY, Rao DA, and Raychaudhuri S (2017). Leveraging blood and tissue CD4+ T cell heterogeneity at the single cell level to identify mechanisms of disease in rheumatoid arthritis. Curr. Opin. Immunol 49, 27–36. [PubMed: 28888129]

Fonseka CY, Rao DA, Teslovich NC, Korsunsky I, Hannes SK, Slowikowski K, Gurish MF, Donlin LT, Lederer JA, Weinblatt ME, et al. (2018). Mixed-effects association of single cells identifies an expanded effector CD4+ T cell subset in rheumatoid arthritis. Sci. Transl. Med 10, 10.

Gnoni GV, Priore P, Geelen MJ, and Siculella L (2009). The mitochondrial citrate carrier: metabolic role and regulation of its activity and expression. IUBMB Life 61, 987–994. [PubMed: 19787704]

Goronzy JJ, and Weyand CM (2017). Successful and Maladaptive T Cell Aging. Immunity 46, 364–378. [PubMed: 28329703]

Hassan BH, and Cronan JE (2011). Protein-protein interactions in assembly of lipoic acid on the 2-oxoacid dehydrogenases of aerobic metabolism. J. Biol. Chem 286, 8263–8276. [PubMed: 21209092]

Hind LE, Vincent WJ, and Huttenlocher A (2016). Leading from the Back: The Role of the Uropod in Neutrophil Polarization and Migration. Dev. Cell 38, 161–169. [PubMed: 27459068]

Icard P, Poulain L, and Lincet H (2012). Understanding the central role of citrate in the metabolism of cancer cells. Biochim. Biophys. Acta 1825, 111–116. [PubMed: 22101401]

Janke C, and Montagnac G (2017). Causes and Consequences of Microtubule Acetylation. Curr. Biol 27, R1287–R1292. [PubMed: 29207274]

Johnson JD, Mehus JG, Tews K, Milavetz BI, and Lambeth DO (1998). Genetic evidence for the expression of ATP- and GTP-specific succinyl-CoA synthetases in multicellular eucaryotes. J. Biol. Chem 273, 27580–27586. [PubMed: 9765291]

Katayama M, Zhong Z, Lai L, Sutovsky P, Prather RS, and Schatten H (2006). Mitochondrial distribution and microtubule organization in fertilized and cloned porcine embryos: implications for developmental potential. Dev. Biol 299, 206–220. [PubMed: 16945363]

Konishi Y, and Setou M (2009). Tubulin tyrosination navigates the kinesin-1 motor domain to axons. Nat. Neurosci 12, 559–567. [PubMed: 19377471]

Lämmermann T, and Sixt M (2009). Mechanical modes of 'amoeboid' cell migration. Curr. Opin. Cell Biol 21, 636–644. [PubMed: 19523798]

Li Y, Shen Y, Hohensinner P, Ju J, Wen Z, Goodman SB, Zhang H, Goronzy JJ, and Weyand CM (2016). Deficient Activity of the Nuclease MRE11A Induces T Cell Aging and Promotes Arthritogenic Effector Functions in Patients with Rheumatoid Arthritis. Immunity 45, 903–916. [PubMed: 27742546]

Li Y, Shen Y, Jin K, Wen Z, Cao W, Wu B, Wen R, Tian L, Berry GJ, Goronzy JJ, and Weyand CM (2019). The DNA Repair Nuclease MRE11A Functions as a Mitochondrial Protector and Prevents T Cell Pyroptosis and Tissue Inflammation. Cell Metab 30, 477–492.e6. [PubMed: 31327667]

Matsuyama A, Shimazu T, Sumida Y, Saito A, Yoshimatsu Y, Seigneurin-Berny D, Osada H, Komatsu Y, Nishino N, Khochbin S, et al. (2002). *In vivo* destabilization of dynamic microtubules by HDAC6-mediated deacetylation. EMBO J 21, 6820–6831. [PubMed: 12486003]

Peng M, Yin N, Chhangawala S, Xu K, Leslie CS, and Li MO (2016). Aerobic glycolysis promotes T helper 1 cell differentiation through an epigenetic mechanism. Science 354, 481–484. [PubMed: 27708054]

Portran D, Schaedel L, Xu Z, Théry M, and Nachury MV (2017). Tubulin acetylation protects long-lived microtubules against mechanical ageing. Nat. Cell Biol 19, 391–398. [PubMed: 28250419]

Quintana A, Schwarz EC, Schwindling C, Lipp P, Kaestner L, and Hoth M (2006). Sustained activity of calcium release-activated calcium channels requires translocation of mitochondria to the plasma membrane. J. Biol. Chem 281, 40302–40309. [PubMed: 17056596]

Rao DA, Gurish MF, Marshall JL, Slowikowski K, Fonseka CY, Liu Y, Donlin LT, Henderson LA, Wei K, Mizoguchi F, et al. (2017). Pathologically expanded peripheral T helper cell subset drives B cells in rheumatoid arthritis. Nature 542, 110–114. [PubMed: 28150777]

Sadoul K, and Khochbin S (2016). The growing landscape of tubulin acetylation: lysine 40 and many more. Biochem. J 473, 1859–1868. [PubMed: 27354562]

Schwindling C, Quintana A, Krause E, and Hoth M (2010). Mitochondria positioning controls local calcium influx in T cells. J. Immunol 184, 184–190. [PubMed: 19949095]

Shen Y, Wen Z, Li Y, Matteson EL, Hong J, Goronzy JJ, and Weyand CM (2017). Metabolic control of the scaffold protein TKS5 in tissue-invasive, proinflammatory T cells. Nat. Immunol 18, 1025–1034. [PubMed: 28737753]

Slowikowski K, Wei K, Brenner MB, and Raychaudhuri S (2018). Functional genomics of stromal cells in chronic inflammatory diseases. Curr. Opin. Rheumatol 30, 65–71. [PubMed: 28984647]

Terao C, Raychaudhuri S, and Gregersen PK (2016). Recent Advances in Defining the Genetic Basis of Rheumatoid Arthritis. Annu. Rev. Genomics Hum. Genet 17, 273–301. [PubMed: 27216775]

Vysochan A, Sengupta A, Weljie AM, Alwine JC, and Yu Y (2017). ACSS2-mediated acetyl-CoA synthesis from acetate is necessary for human cytomegalovirus infection. Proc. Natl. Acad. Sci. USA 114, E1528–E1535. [PubMed: 28167750]

Ward PS, Patel J, Wise DR, Abdel-Wahab O, Bennett BD, Coller HA, Cross JR, Fantin VR, Hedvat CV, Perl AE, et al. (2010). The common feature of leukemia-associated IDH1 and IDH2 mutations is a neomorphic enzyme activity converting alpha-ketoglutarate to 2-hydroxyglutarate. Cancer Cell 17, 225–234. [PubMed: 20171147]

Wellen KE, Hatzivassiliou G, Sachdeva UM, Bui TV, Cross JR, and Thompson CB (2009). ATP-citrate lyase links cellular metabolism to histone acetylation. Science 324, 1076–1080. [PubMed: 19461003]

Wen Z, Jin K, Shen Y, Yang Z, Li Y, Wu B, Tian L, Shoor S, Roche NE, Goronzy JJ, and Weyand CM (2019). N-myristoyltransferase deficiency impairs activation of kinase AMPK and promotes synovial tissue inflammation. Nat. Immunol 20, 313–325. [PubMed: 30718913]

Weyand CM, and Goronzy JJ (2006). T-cell-targeted therapies in rheumatoid arthritis. Nat. Clin. Pract. Rheumatol 2, 201–210. [PubMed: 16932686]

Weyand CM, and Goronzy JJ (2020). Immunometabolism in the development of rheumatoid arthritis. Immunol. Rev 294, 177–187. [PubMed: 31984519]

Weyand CM, Zeisbrich M, and Goronzy JJ (2017). Metabolic signatures of T-cells and macrophages in rheumatoid arthritis. Curr. Opin. Immunol 46, 112–120. [PubMed: 28538163]

Xu Z, Schaedel L, Portran D, Aguilar A, Gaillard J, Marinkovich MP, Théry M, and Nachury MV (2017). Microtubules acquire resistance from mechanical breakage through intralumenal acetylation. Science 356, 328–332. [PubMed: 28428427]

Yang Z, Fujii H, Mohan SV, Goronzy JJ, and Weyand CM (2013). Phosphofructokinase deficiency impairs ATP generation, autophagy, and redox balance in rheumatoid arthritis T cells. J. Exp. Med 210, 2119–2134. [PubMed: 24043759]

Yang Z, Shen Y, Oishi H, Matteson EL, Tian L, Goronzy JJ, and Weyand CM (2016). Restoring oxidant signaling suppresses proarthritogenic T cell effector functions in rheumatoid arthritis. Sci. Transl. Med 8, 331ra38.

Zhang F, Wei K, Slowikowski K, Fonseka CY, Rao DA, Kelly S, Goodman SM, Tabechian D, Hughes LB, Salomon-Escoto K, et al.; Accelerating Medicines Partnership Rheumatoid Arthritis and Systemic Lupus Erythematosus (AMP RA/SLE) Consortium (2019). Defining inflammatory cell states in rheumatoid arthritis joint synovial tissues by integrating single-cell transcriptomics and mass cytometry. Nat. Immunol 20, 928–942. [PubMed: 31061532]

## Highlights

- T cells deficient in succinyl-CoA ligase (SUCLG2) accumulate acetyl-CoA
- Excess acetyl-CoA promotes protein acetylation, stabilizing microtubules
- Tubulin hyperacetylation amplifies T cell uropod formation and tissue invasiveness
- SUCLG2-deficient T cells are proinflammatory, inflicting rheumatoid synovitis

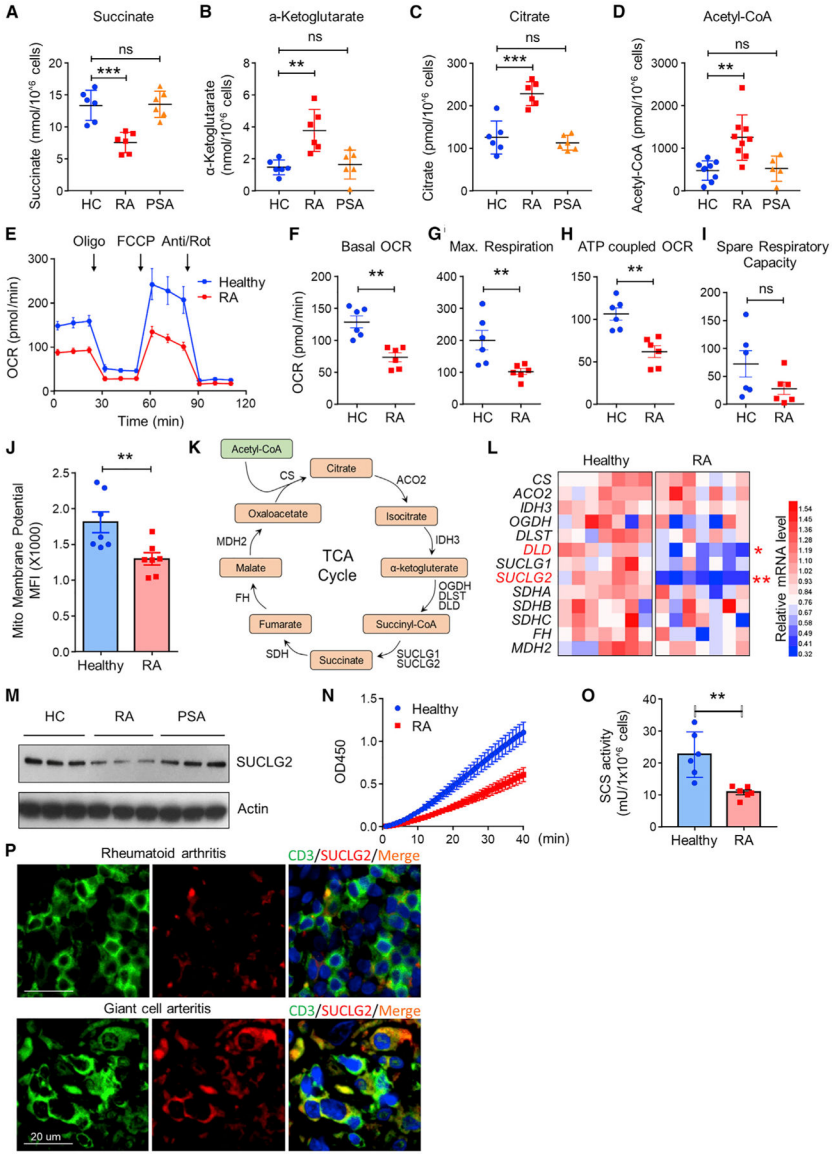


**Figure 1. Repression of the Mitochondrial Enzyme Succinate-CoA Ligase (SUCLG2) in RA T Cells**

$CD4^+CD45RA^+$ T cells from patients with rheumatoid arthritis (RA), patients with psoriatic arthritis (PsA), and age-matched healthy individuals were stimulated for 72 h.

(A–D) Intracellular concentrations of the mitochondrial metabolites succinate, α-KG, citrate, and acetyl-CoA.

(E–I) Mitochondrial oxygen consumption rates (OCR) measured by Seahorse Analyzer.

(E) Summary OCR traces from healthy (n = 6, blue) and RA T cells (n = 6, red).

(F–I) Baseline respiration (F), maximal respiration (G), ATP-coupled respiration (H), and spare respiratory capacity (I) were calculated.

(J) Mitochondrial membrane potential measured by flow cytometry for MitoTracker Red. MFIs from six controls and six RA patients.

(K) Scheme illustrating enzymes and metabolic intermediates in the TCA cycle.

(L) Transcripts of 13 TCA cycle enzymes quantified by RT-PCR. Heatmap presentation from seven healthy-RA pairs. p values and significance levels adjusted for multiple comparisons.

(M) Immunoblot analysis of Succinate-CoA Ligase GDP-Forming Beta Subunit (SUCLG2) in T cells from three RA patients, three PsA patients, and three healthy controls.

(N and O) Succinyl-CoA synthetase activity in healthy and RA T cells. Real-time OD values indicating the catalytic reaction (N). Calculated SCS activity of six healthy and six RA T cell samples (O).

(P) Double immunofluorescence staining for CD3 and SUCLG2 in tissue sections from rheumatoid synovitis (top) and giant cell arteritis (bottom).

Scale bar; 20 μm. Data are mean ± SEM. One-way ANOVA and post-ANOVA pairwise two-group comparisons conducted with Tukey's method (A–D). Unpaired Mann-Whitney-Wilcoxon rank test (F–J, L, O). *$p < 0.05$, **$p < 0.01$, ***$p < 0.001$.

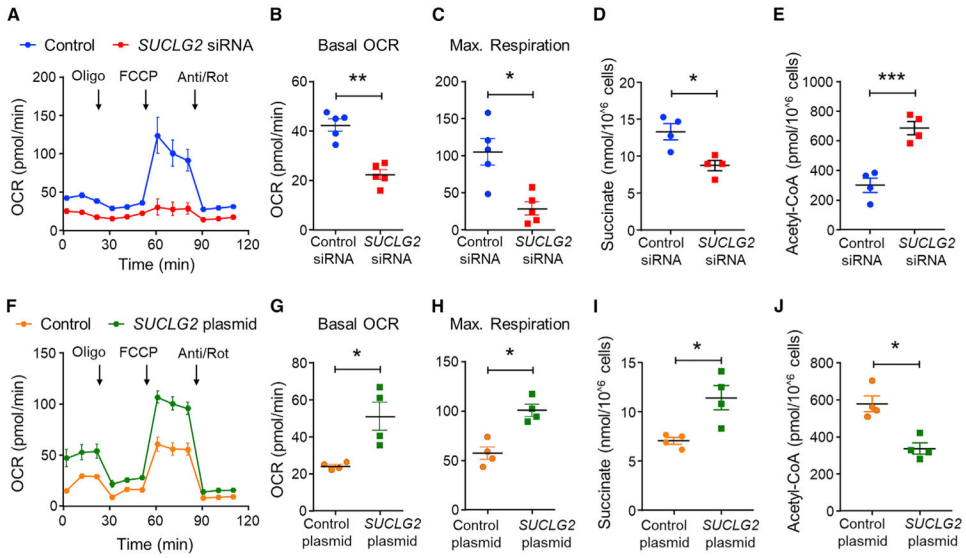


**Figure 2. Succinate-CoA Ligase (SUCLG2) Regulates Mitochondrial Activity and the Intracellular Acetyl-CoA Pool**

$CD4^+CD45RA^+$ T cells from healthy individuals and RA patients were stimulated for 48 h. *SUCLG2* was knocked down in healthy T cells by siRNA transfection or overexpressed in RA T cells by plasmid transfection. Cells were examined 48 h later.

(A–C) Oxygen consumption rates (OCR) measured by Seahorse analyzer.

(A) OCR traces after transfection of control siRNA or *SUCLG2* siRNA (n = 5).

(B and C) Baseline and maximal respiration were calculated.

(D and E) Intracellular succinate and AcCoA concentrations in healthy T cells after *SUCLG2* knockdown (n = 4).

(F–H) *SUCLG2* was overexpressed in RA CD4 T cells, and mitochondrial oxygen consumption rates (OCR) were measured by Seahorse analyzer.

(F) Summary OCR curves from four experiments.

(G and H) Baseline and maximal respiration were calculated.

(I and J) Intracellular succinate and AcCoA concentrations after *SUCLG2* overexpression in RA CD4 T cells (n = 4).

Data are mean ± SEM. Paired t test. *p < 0.05, **p < 0.01, ***p < 0.001.

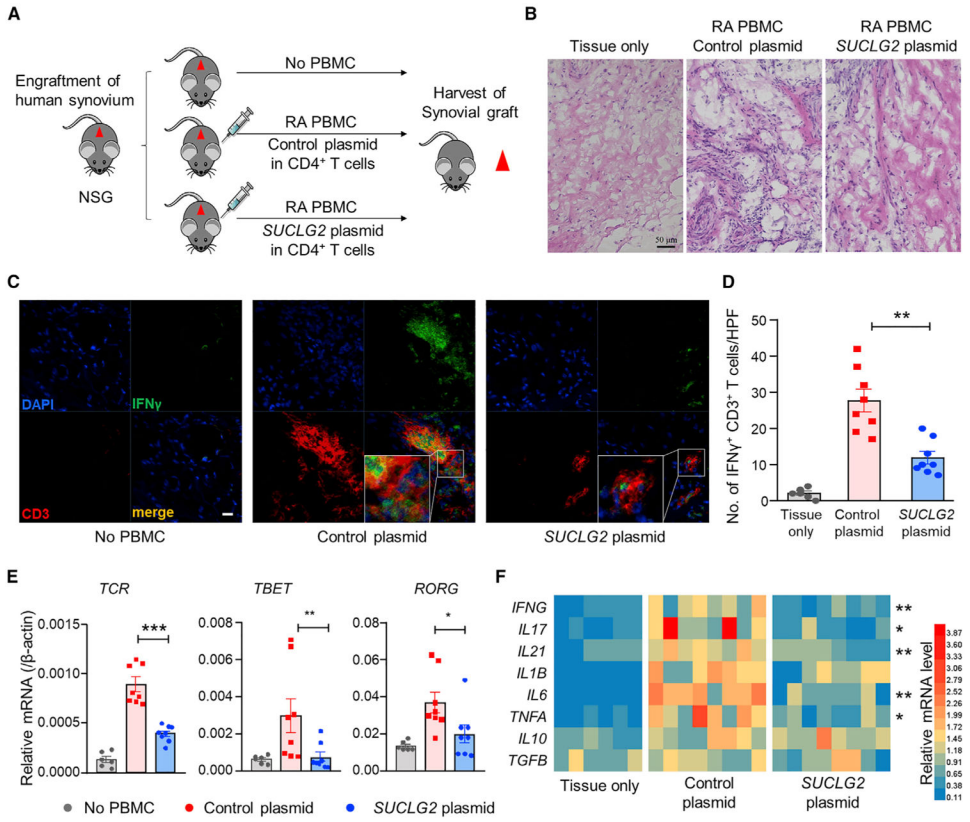


**Figure 3. The Mitochondrial Enzyme SUCLG2 Is Tissue Protective**

NSG mice were engrafted with human synovial tissue and immune-reconstituted with RA PBMCs. Prior to the adoptive transfer into the NSG mice, CD4 T cells were FACS-sorted and transfected with a control or *SUCLG2* overexpression plasmid.

(A) Experimental scheme. Human synovium-NSG mice were divided into three groups: no PBMC injection (n = 6), RA PBMCs (CD4 T cells transfected with control plasmid) injection (n = 8), RA PBMCs (CD4 T cells transfected with *SUCLG2* plasmid) injection (n = 8).

(B) H&E staining of synovial tissue sections.

(C) Immunofluorescence co-staining for IFN-γ and CD3 in synovial explants. Representative images; scale bar, 10 μm.

(D) Enumeration of tissue-residing IFN-$\gamma^+$ $CD3^+$ T cells in each synovial explant. Average IFN-$\gamma^+$ $CD3^+$ T cell numbers calculated from 3 HPF.

(E) *TRB, TBET*, and *RORG* transcripts in tissue extracts measured by RT-PCR.

(F) Gene expression profiling (RT-PCR) of key inflammatory markers.

Data are mean ± SEM. Unpaired Mann-Whitney-Wilcoxon rank test. *p < 0.05, **p < 0.01, ***p < 0.001.

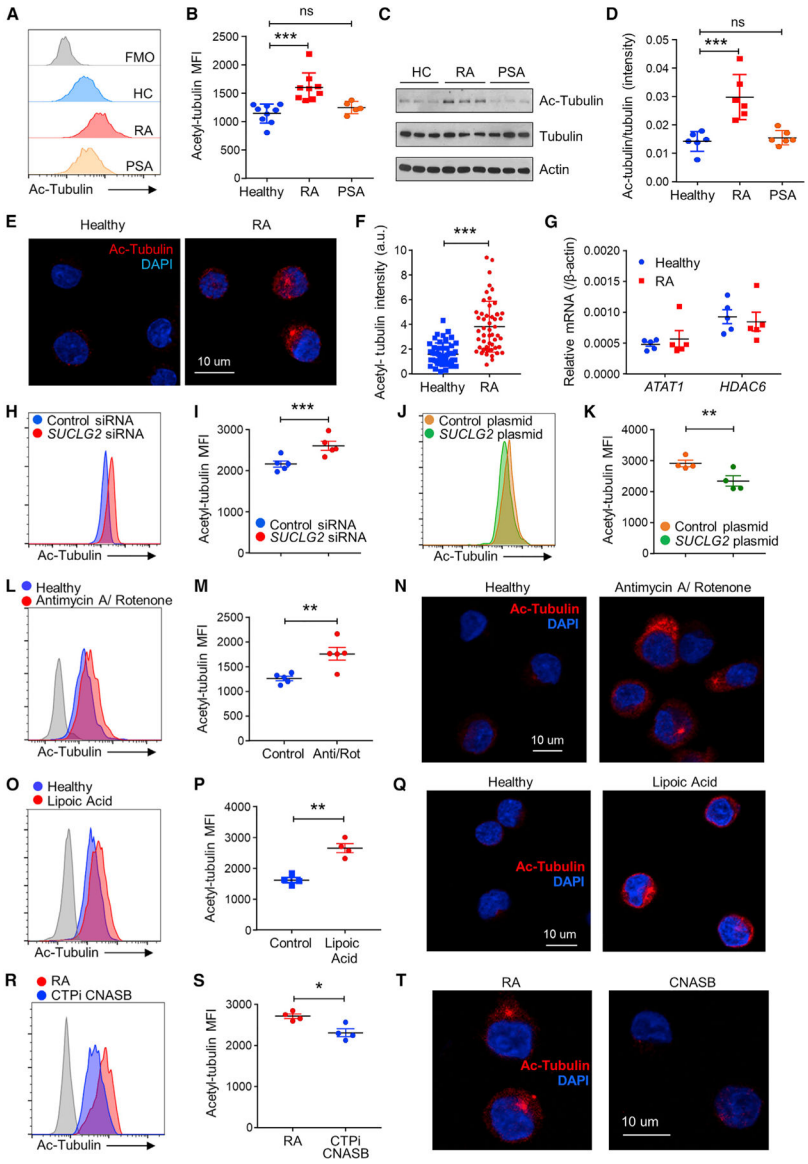


**Figure 4. Tubulin Is Hyperacetylated in RA T Cells**

$CD4^+CD45RA^+$ T cells from patients and controls were stimulated for 72 h as in Figure 1.

(A and B) Cytofluorometric analysis of tubulin acetylation.

(A) Representative histograms.

(B) MFIs from eight RA patients, five PsA patients, and nine controls.

(C and D) Immunoblot analysis of tubulin acetylation in six RA patients, six PsA patients, and six controls.

(C) Representative blot data.

(D) Quantification of blot intensity.

(E) Confocal imaging of acetylated tubulin. Representative images. Scale bars, 10 μm.

(F) Fluorescence intensity quantification from 50 cells in 5 control and 5 RA samples.

(G) *ATAT1* and *HDAC6* transcripts in five control-RA pairs measured by RT-PCR.

(H and I) Flow cytometry of acetylated tubulin in healthy CD4 T cells transfected with control siRNA or *SUCLG2* siRNA.
(H) Representative histogram.
(I) MFIs from five healthy samples.
(J and K) Tubulin acetylation in RA CD4 T cells after *SUCLG2* overexpression. Representative histograms and MFIs from four RA samples.
(L and M) Tubulin acetylation in healthy CD4 T cells treated with Antimycin A/Rotenone (5 nM). Representative histograms and MFIs from five samples.
(N) Representative confocal microscopy image of Ac-tubulin. Scale bars, 10 μm.
(O–Q) Cytofluorometry and confocal microscopy of Ac-tubulin in CD4 T cells treated with lipoic acid (500 μM).
(O and P) Representative histograms and MFIs from four samples.
(Q) Representative confocal image showing Ac-tubulin. Scale bars, 10 μm.
(R–T) Tubulin acetylation in RA T cells treated with the mitochondrial citrate transport protein (CTP) inhibitor CNASB (250 μM).
(R and S) Representative histograms and MFIs from four RA samples.
(T) Representative confocal picture Ac-tubulin in CNASB-treated RA T cells. Scale bars, 10 μm.
Data are mean ± SEM. One-way ANOVA and post-ANOVA pairwise two-group comparisons conducted with Tukey's method (B, D). Unpaired Mann-Whitney-Wilcoxon rank test (F, G). Paired t test (I, K, M, P, S). *$p < 0.05$, **$p < 0.01$, ***$p < 0.001$.

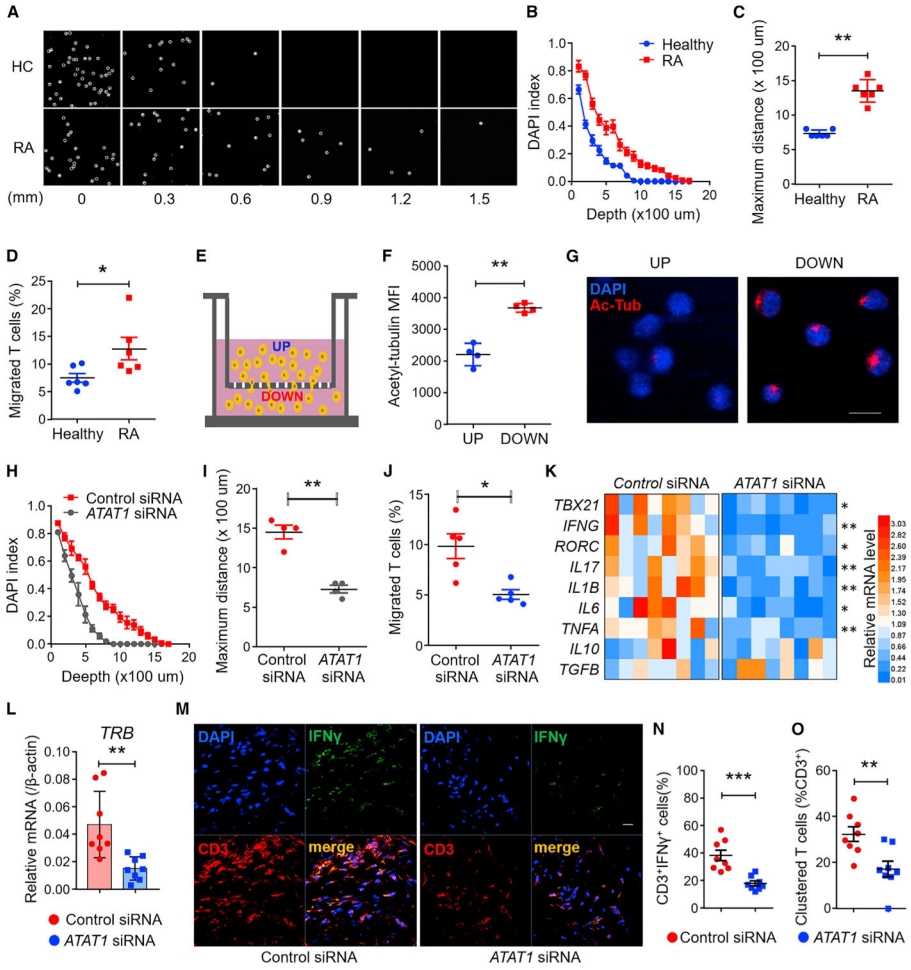


**Figure 5. Tubulin Hyperacetylation Promotes T Cell Mobility**

$CD4^+CD45RA^+$ T cells from patients and controls were stimulated for 72 h.

(A–C) CD4 T cell invasiveness in 3D collagen matrices, measured by confocal microscopy for DAPI-stained nuclei. (n = 6 HC-RA pairs).

(A) Representative confocal images at the indicated depths after 48 h. Cells are marked by circles.

(B) DAPI indices (signal at defined depth/surface signal).

(C) Maximum invasion distances of healthy and RA T cells.

(D) Migration of activated CD4 T cells in transwells without chemokines for 24 h (n = 6 HC-RA pairs).

(E–G) T cells from the upper and lower chambers stained for Ac-tubulin.

(E) Schematic diagram.

(F) MFI of Ac-tubulin measured by flow cytometry (n = 4 up-down pairs).

(G) Representative confocal images of T cells from the upper and lower chambers stained for Ac-tubulin.

(H and I) CD4 T cell invasiveness in 3D collagen matrices after *ATAT1* knockdown in RA T cells (n = 4).

(H) DAPI indices (signal at defined depth/surface signal).

(I) Maximum invasion distances.

(J) Percentage of migrated T cells in transwell assays after *ATAT1* knockdown in RA T cells (n = 5).

(K–O) NSG mice engrafted with human synovial tissue were reconstituted with RA PBMCs that had been transfected with control or *ATAT1* siRNA. Immunohistochemical staining and tissue transcriptome analysis was performed in explanted synovial grafts. Eight tissues in each group.

(K) Gene expression profiling of key inflammatory markers.

(L) *TRB* mRNA measured by RT-PCR.

(M) Co-immunofluorescence staining for IFN-γ and CD3 in synovial explants. Representative images, scale bar; 10 μm.

(N) Frequencies of tissue-residing $CD3^{+}$IFN-$\gamma^{+}$ T cells.

(O) Percentage of tissue $CD3^{+}$ T cells that form clusters.

All data are mean ± SEM. Unpaired Mann-Whitney-Wilcoxon rank test (C, D, K–O). Paired t test (F, I, J). *p < 0.05, **p < 0.01, ***p < 0.001.

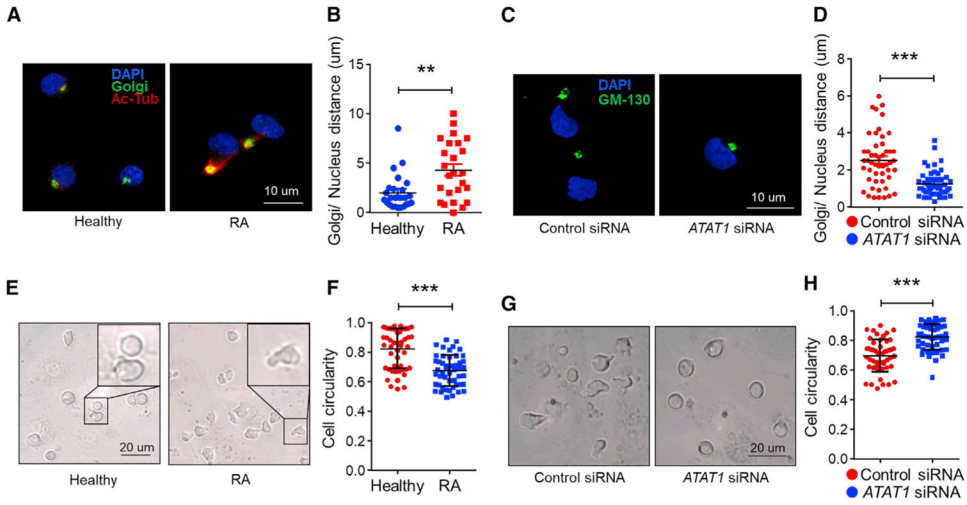


**Figure 6. Tubulin Hyperacetylation Promotes T Cell Uropod Formation**

$CD4^+CD45RA^+$ T cells from patients and controls were stimulated for 72 h and seeded on collagen-coated surfaces (A–D) or on endothelial cell (EC) monolayers (E–H).

(A and B) Co-immunofluorescence staining for the Golgi marker GM-130 (green), Ac-tubulin (red), and nuclei (DAPI).

(A) Representative micrographs.

(B) Quantification of the Golgi-to-nucleus distance. 50 cells from 5 healthy samples and 5 RA samples were analyzed.

(C and D) RA CD4 T cells were transfected with *CONTROL* or *ATAT1* siRNA and stained for GM-130 (green). Nuclei marked with DAPI.

(C) Representative micrographs.

(D) Quantification of the Golgi-to-nucleus distance in spreading RA CD4 T cells after *ATAT1* knockdown (n = 5).

(E and F) Quantification of T cell circularity in control and RA T cells. Representative images and analysis of ten cells from each sample in five healthy-RA pairs.

(G and H) Representative micrographs and quantification of cell circularity in spreading T cells after *ATAT1* knockdown (n = 5, 10 cells from each sample).

All data are mean ± SEM. Unpaired Mann-Whitney-Wilcoxon rank test (B, F, H). $^{**}p < 0.01$, $^{***}p < 0.001$.

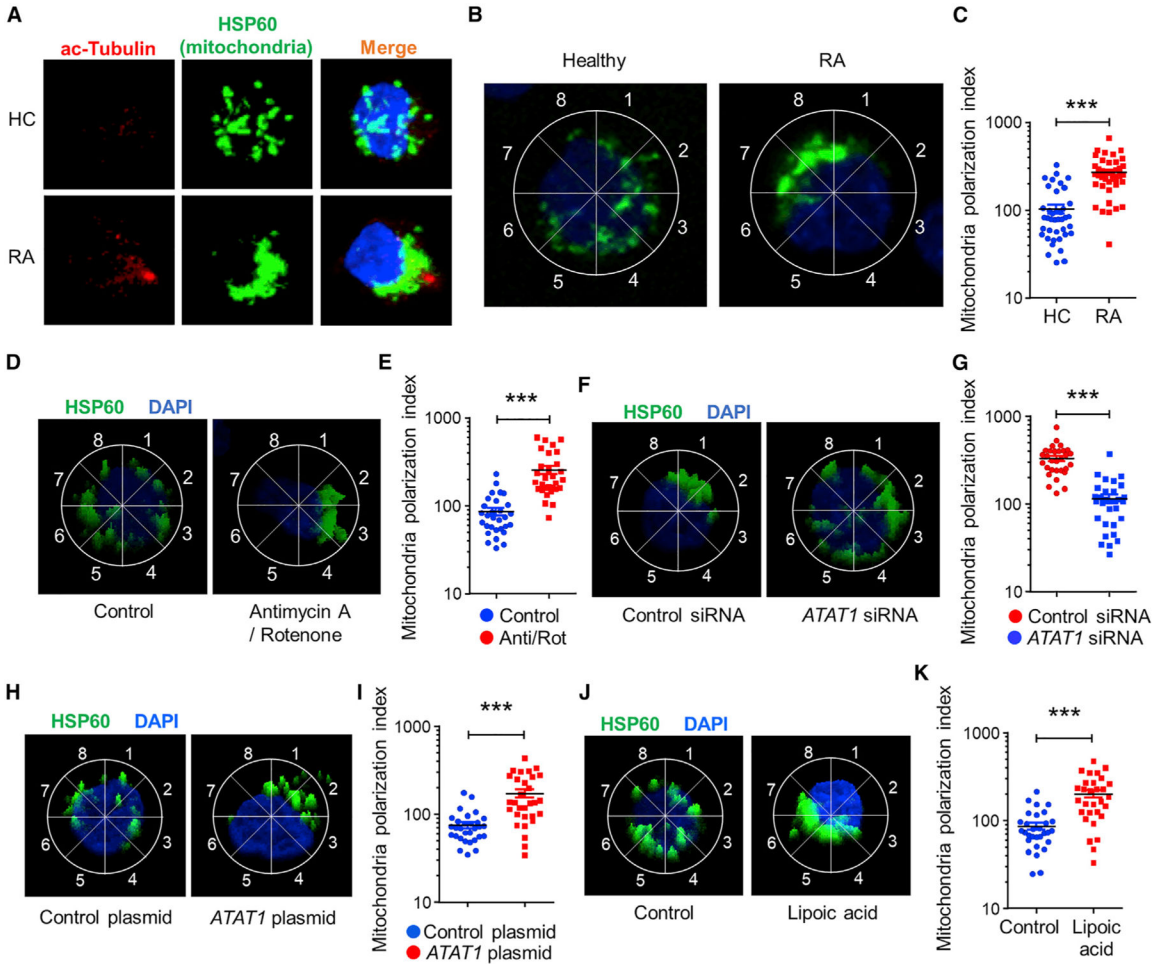


**Figure 7. Tubulin Hyperacetylation Leads to Mitochondrial Clustering in RA CD4 T Cells**

$CD4^+CD45RA^+$ T cells from RA patients and controls were activated for 72 h and stained for the mitochondrial marker HSP60. Nuclei were marked with DAPI.

(A) Representative confocal images (3D Maximum mode) of ac-tubulin and HSP60 staining.

(B) Confocal microscopy of individual cells stained for HSP60. Fluorescence was quantified in each of eight parts.

(C) Mitochondria polarization index of healthy and RA T cells. 40 cells from 4 healthy samples and 40 cells from 4 RA samples were analyzed.

(D and E) Representative microscopy images of HSP60 staining (D) and mitochondria polarization indices (E) in healthy T cells treated with the mitochondrial inhibitor Antimycin A/Rotenone (5 nM). 60 cells from 3 samples were evaluated.

(F and G) Representative images of HSP60 staining (F) and mitochondria polarization indices (G) in RA T cells transfected with control or ATAT1 siRNA. 60 cells from 3 RA samples.

(H and I) Representative microscopy images of HSP60 staining (H) and mitochondria polarization indices (I) after *ATAT1* overexpression in healthy T cells. 60 cells from 3 samples.

(J and K) Representative microscopy images of HSP60 staining (J) and mitochondria polarization indices (K) in healthy T cells treated with lipoic acid (500 μM). 60 cells from 3 samples.

All data are mean ± SEM. Unpaired Mann-Whitney-Wilcoxon rank test. ***$p < 0.001$.

## KEY RESOURCES TABLE

| REAGENT or RESOURCE | SOURCE | IDENTIFIER |
|---|---|---|
| Antibodies | | |
| Mouse monoclonal anti-SUCLG2 (A-2) | Santa Cruz Bio | Cat#sc-390818 |
| Mouse monoclonal anti-CD3 | Dako | Cat#M725401–2 |
| Rabbit polyclonal anti-Interferon gamma | Abcam | Cat#ab25101, RRID:AB_448613 |
| Mouse monoclonal anti-Acetyl-alpha Tubulin (Lys40) | Thermo Fisher Scientific | Cat#32–2700, RRID:AB_2533073 |
| Rabbit monoclonal anti-alpha Tubulin | Cell Signaling Technology | Cat#2125, RRID:AB_2619646 |
| Rabbit monoclonal anti-GM130 | Cell Signaling Technology | Cat#12480S, RRID:AB_2797933 |
| Rabbit monoclonal anti-HSP60 | Cell Signaling Technology | Cat#12165S, RRID:AB_2636980 |
| Rabbit polyclonal anti-Pericentrin | Abcam | Cat#ab4448, RRID:AB_304461 |
| Mouse monoclonal anti-b-Actin | Cell Signaling Technology | Cat#3700S, RRID:AB_2242334 |
| Brilliant Violet 421 anti-human IFN-γ | BioLegend | Cat#502532, RRID:AB_2561398 |
| PE anti-human IL-17A | BioLegend | Cat# 512306, RRID:AB_961394 |
| Goat anti-rabbit IgG (H+L), Alexa Fluor 488 | Thermo Fisher Scientific | Cat#A-11008, RRID:AB_143165 |
| Goat anti-mouse IgG (H+L), Alexa Fluor 594 | Thermo Fisher Scientific | Cat#A-11032, RRID:AB_2534091 |
| Biological Samples | | |
| PBMC from healthy donors | Stanford Blood Center | N/A |
| PBMC from patients | Stanford University | N/A |
| Human synovial tissue | Stanford University | N/A |
| Chemicals, Peptides, and Recombinant Proteins | | |
| Anti-CD3/CD28 beads | Life Technologies | Cat#11132D |
| Lymphorep | Cosmo Bio | Cat#AXS-1115758 |
| 4% paraformaldehyde | Santa Cruz Bio | Cat#sc-281692 |
| a-Lipoic acid | Sigma-Aldrich | Cat#T1395 |
| CTP Inhibitor | Sigma-Aldrich | Cat#SML0068 |
| Nocodazole | Abcam | Cat#ab120630 |
| Bovine Type I Collagen Solution | Advanced Biomatrix | Cat#5005-100ML |
| Rhodamine Phalloidin | Thermo Fisher Scientific | Cat#R415 |
| BODIPY 493/503 | Thermo Fisher Scientific | Cat#D3922 |
| DAPI | Cayman | Cat#14285 |
| Cell Activation Cocktail | BioLegend | Cat#423301 |
| Brefeldin A Solution | BioLegend | Cat#420601 |
| Recombinant Human TNF-a | BioLegend | Cat#717904 |
| Sodium acetate | Sigma-Aldrich | Cat#S2889 |
| RPMI 1640 Medium | Thermo Fisher Scientific | Cat#11875135 |
| 4–15% SDS-PAGE | Bio-Rad | Cat#4561083 |
| PVDF membranes | Bio-Rad | Cat#1620177 |
| TBST | Cell Signaling Technology | Cat#9997S |

| REAGENT or RESOURCE | SOURCE | IDENTIFIER |
|---|---|---|
| PBS | Boston BioProducts | Cat#BM-220 |
| Tris-Glycine-SDS Running Buffer (10X) | Boston BioProducts | Cat#NBP-150 |
| Tris-Glycine Transfer Buffer (10X) #12539 | Cell Signaling Technology | Cat#12539S |
| SuperSignal West Femto Maximum Sensitivity Substrate | Thermo Fisher Scientific | Cat#34094 |
| Direct-zol RNA MiniPrep | Genesee Scientific | Cat#11-331 |
| High-Capacity cDNA Reverse Transcription Kit | Thermo Fisher Scientific | Cat#4368813 |
| 2x SYBR Green qPCR Master Mix | Bimake | B21203 |
| Critical Commercial Assays | | |
| Human Naive CD4+ T Cell Isolation Kit | StemCell Technologies, Inc. | Cat#17555 |
| Succinate Assay Kit | BioAssay Systems | Cat#ESNT-100 |
| Alpha-Ketoglutarate Assay Kit | BioVision | Cat#K677-100 |
| Citrate Assay Kit | Sigma-Aldrich | Cat#MAK057-1KT |
| Acetyl-Coenzyme a Assay Kit | Sigma-Aldrich | Cat#MAK039-1KT |
| Succinyl-CoA Synthetase Activity Assay Kit | BioVision | Cat#K597-100 |
| Free Fatty Acid Quantification Assay Kit | Abcam | Cat#ab65341 |
| MitoTracker Red | Invitrogen | Cat#M7512 |
| Seahorse XF Cell Mito Stress Test Kit | Agilent Technologies | Cat#103015-100 |
| Transwell with 3.0 μm Pore Polyester Membrane Insert | Corning | Cat#3462 |
| Hematoxylin & Eosin Stain Kit | Vector Laboratories | Cat#H-3502 |
| Experimental Models: Cell Lines | | |
| HUVEC | ATCC | Cat#PCS-100-010 |
| Experimental Models: Organisms/Strains | | |
| NSG mice | The Jackson Laboratory | Stock#005557 |
| Oligonucleotides | | |
| *SUCLG2* siRNA | Dharmacon | Cat#L-008918-01-0005 |
| *SUCLG2* siRNA #2 | Santa Cruz Bio | Cat#sc-77883 |
| *ATAT1* siRNA | Thermo Fisher Scientific | Cat# 4392420 |
| Recombinant DNA | | |
| *SUCLG2* cDNA ORF clone, Homo sapiens(human) | GenScript | Cat#OHu94733 |
| *ATAT1* cDNA ORF clone, Homo sapiens(human) | GenScript | Cat#OHu20743 |
| Software and Algorithms | | |
| FlowJo | BD | https://www.flowjo.com/ |
| ImageJ | NIH | https://imagej.nih.gov/ij/ |
| GraphPad Prism | GraphPad Software | https://www.graphpad.com/scientific-software/prism/ |
| ZEN 2010 software | Carl Zeiss | https://www.zeiss.com/microscopy/us/products/microscope-software/zen-lite.html |

| REAGENT or RESOURCE | SOURCE | IDENTIFIER |
|---|---|---|
| Seahorse Wave Controller software | Seahorse/Agilent | https://www.agilent.com/en/products/cell-analysis/cell-analysis-software/instrument-software/wave-controller-2-4 |